Seismic Deformation Analysis of Precast Concrete Pipe Hybrid Based on 3D LiDAR and Unmanned Aerial Vehicle Photogrammetry

Ming Guo,[1,2] Xuanshuo Liang,[1] Youshan Zhao,[3,4,*] Guoli Wang,[1] and Kecai Guo[5]

[1]School of Geomatics and Urban Spatial Informatics, Beijing University of Civil Engineering and Architecture, Beijing 102616, China
[2]Key Laboratory of Modern Urban Surveying and Mapping, National Administration of Surveying, Beijing 100044, China
[3]China Academy of Building Research, Beijing 100013, China
[4]CABR Testing Center Co., Ltd., Beijing 100013, China
[5]Beijing Shenxin Reach Technology Co., Ltd., Beijing 102444, China

In this study, we utilized unmanned aerial vehicle (UAV) and high-precision 3D light detection and ranging (LiDAR) scanning to collect data before and after an earthquake-resistant behavior test on a reinforced concrete hybrid frame. We analyzed the deformation of the hybrid frame before and after the test and determined the specific deformation, scale, and change rule. The UAV image data was transformed into a 3D true-color model using the structure from motion (SfM) algorithm. Additionally, the 3D Delaunay surface reconstruction algorithm was used to create a 3D point cloud model and Rodriguez matrix, which are then used to align the two-phase model. Subsequently, a comparison was made in three dimensions between the distribution of the hybrid frame's photographic and 3D point cloud models before and after undergoing earthquake-resistant behavior tests. This method allows for a precise analysis of the local deformation degree of the hybrid frame structure compared with the sensors. While the sensors can only analyze internal structural changes, this method provides results for both local and surface deformation degrees, which are not available in the sensor data. The comprehensive experimental comparison results demonstrate that the reinforced concrete hybrid frame structure had a collective rightward displacement before and after the earthquake-resistant behavior test. Moreover, nodes and edges exhibited more significant deformation, and the test resulted in a more stable overall framework.

1. Introduction

The reinforced concrete structure (RCS) hybrid frame comprises reinforced concrete (RC) columns and beams, the reinforced concrete structure of which refers to the structure built of

---

concrete strengthened through steel reinforcement. RC columns offer substantial resistance to lateral forces, whereas steel beams exhibit favorable behavior in earthquake scenarios. These characteristics align with the demands of contemporary construction technology, as outlined by various national and international organizations since the early 1980s. The United States initiated developing the RCS hybrid frame system, which combines traditional RC frame, steel, and steel-framed concrete structures. This system has been effectively implemented in medium- and high-rise buildings. Subsequently, RCS buildings have gained extensive utilization in the global construction industry. To attain the desired levels of design strength and durability, it is necessary to employ suitable building techniques.[1] Owing to the frequent occurrence of natural disasters around the world, the seismic performance of RCS in various natural disasters, especially in earthquake disasters, plays a decisive role in the safety of residents; thus, it is necessary to study the seismic performance of RCS. At present, a variety of studies have been carried out, including but not limited to the use of fiber reinforcement in RCS to improve the structural performance,[2,3] the new connection method of steel-beam wrapped concrete composite columns,[4] the analysis of structural deformation[1,5] in the experiment of RCS, and the evaluation of the performance of trapezoidal corrugated web reduced beam section connection under cyclic load.[6]

The subject of this study is the precast concrete pipe composite column-steel beam hybrid frame. A load-bearing component connects steel beams and concrete pipes using shear-resistant connectors. This structure combines steel's tensile strength and concrete's compressive performance, resulting in high load-bearing capacity, stiffness, earthquake resistance, and dynamic performance. Additionally, it offers the advantages of small cross-sectional size, easy construction, and other benefits. In this study, we combined unmanned aerial vehicle (UAV) photogrammetry and 3D light detection and ranging (LiDAR) scanning technology to collect data on the research object. These methods are commonly used to analyze urban scenes and ancient buildings, and have many other uses such as the quasi-vertical wall of a dam,[7] infrastructure monitoring and bridge evaluation, industrial chimney geometry,[8] and the measurement of towers and churches.[9] However, these methods have not been applied to the analysis of the local deformation of steel structures. In this work, we present an enhanced data acquisition and analysis process that extends the scope of deformation analysis for steel structures beyond sensor data acquisition and finite element analysis.

3D LiDAR scanning is a system that combines three technologies – laser, global positioning system (GPS), and inertial navigation system (INS) – to acquire point cloud data and generate accurate digitized 3D models. The combination of these three technologies allows for the acquisition of a 3D view of the surrounding area with the consistent and absolute measurement of point locations. Utilizing 3D LiDAR scanning technology enables the acquisition of extensive 3D point cloud data on the intricate surfaces of buildings. By analyzing and processing this data, we can comprehensively and precisely understand the building's tilt, settlement,[10,11] and overall deformation. This method is extensively employed in examining and safeguarding distorted structures and the architecture domain. It can be utilized to scrutinize the flaws in the construction of curtain walls,[12] precisely gather data, and conduct a thorough analysis and evaluation of intricate steel structures[13] and substantial steel structures.[14,15] Furthermore, 3D

LiDAR scanning technology can be employed to assess the corrosiveness of the surface of the steel reinforcement[16] and other related applications. Its application before and after an earthquake disaster is also very extensive, and it can extract the seismic characteristics, deformation,[17–19] and distribution of deformed buildings[20] with small deviations that cannot be detected by the naked eye. UAV photogrammetry can be used to capture multiangle target images and correct them with camera orientation, ultimately creating a 3D model that can be used for mapping or terrain analysis. In large-scale construction surveys, UAV photogrammetry can effectively capture features and textures. It can considerably minimize the manual effort required to conduct surveys of historic architectural heritage[21,22] and acquire urban data.[23] The conventional UAV data collection process requires enhanced stability. However, owing to ongoing advancements in science and technology, the device's portability has been enhanced,[24] and its capabilities are progressively expanding, hence alleviating the workload associated with fieldwork. In an earthquake disaster, UAV photogrammetry can generate a dense point cloud[25,26] and combine thermal infrared technology[27] or 3D LiDAR technology to analyze building or terrain deformations[28] in a more sophisticated way to help with earthquake relief and post-disaster reconstruction.

To avoid the problems of partially missing data and unclear characterization caused by a single sensor, we carried out data acquisition and deformation analysis of the manufactured concrete pipe combined column-steel beam hybrid frame based on UAV photogrammetry and 3D LIDAR synergistic observation technology. This study is mainly divided into three phases: program design and data acquisition, experimental data preprocessing, and data analysis. The specific technical roadmap is shown in Fig. 1.

In the program design and data acquisition phase, the overall program design and data acquisition of the research object are combined with the actual situation, which mainly includes
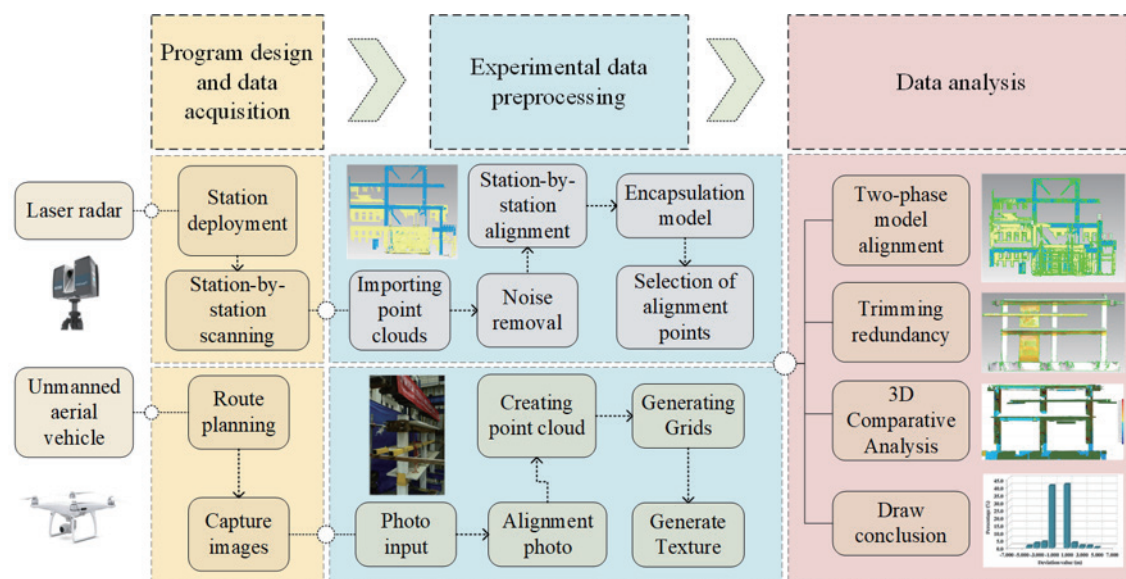

Fig. 1.   (Color online) Research technical route.

the deployment of 3D LIDAR scanning sites and the planning of UAV photogrammetric routes. In the experimental data preprocessing phase, the noise is removed from the 3D LIDAR scanning point cloud, and the 3D model is formed after the encapsulation process of station-by-station alignment.[29] For the true-color 2D images acquired by the UAV, automatic and manual alignments are performed, and to ensure that the data utilization is maximized, 3D reconstruction is performed on the basis of the SfM[30] algorithm. The two models were continuously and repeatedly trimmed, cropped, and aligned on the basis of the Rodriguez matrix algorithm for subsequent deformation analysis. In the data analysis phase, the two data models were analyzed macroscopically and microscopically to determine the specific deformation parts and the degree of deformation in the two data before and after the seismic performance test.

2. Data and Materials

2.1 Study object

The seismic experimental facility is located at Tianjin University in China. A one-bay transverse frame of a four-story dormitory building was selected as the prototype of our experiment. A scaled-down model of an energy-dissipating RCS was designed and built at a ratio of 2/3, consisting of a single story and a single span. The RCS structure is designed with a scale ratio of 1/2, a column spacing of 3 m, a floor height of 1.8 m, a combined beam with a full shear connection of H200 × 100 × 6 × 8, a RC floor slab of 60 mm thickness, and a width of 1100 mm. The designed axial compression ratios are 0.43 for side columns and 0.81 for center columns. The column beam bending capacity ratio, also known as the column end moment reinforcement coefficient, is 1.6, and the structure has a strong node coefficient of 1.38.

The beams and columns in the energy-dissipating substructure are crucial components built to withstand significant forces. The concrete wall in the vertical joints is engineered to provide damping force, taking into account the maximum displacement that may occur. The primary goal of the energy-dissipating substructure is to ensure that the beams and columns remain intact and do not bend during infrequent earthquakes.

Additionally, the core of the beams, columns, and nodes should exhibit shear elasticity. The primary performance goals for vertical seam concrete walls are to maintain their elasticity across several earthquakes and to surrender and dissipate energy during severe and infrequent earthquakes. The primary purpose of implementing a vertical slit slab is to enhance the structural resilience and earthquake resistance of the building. The vertical slit slab serves as a secondary line of defense against seismic activity, specifically targeting the damage sequence of the slab-beam column. However, note that the vertical slit slab alone does not provide all the necessary stiffness; the overall stiffness is achieved through the combined contribution of the frame and vertical slit slab. The structural loading regime involves the joint management of force and displacement. Initially, the loading is force-controlled, and then it transitions to displacement-controlled. The loading process stops when it reaches 85% of the yield load. The loading is intended to be static to intensify the damage process of the components. The duration of the seismic process is typically very brief, approximately 10 s. The experiment complies with

the code for the design of concrete structures (GB 50010-2010) and the code for the seismic design of buildings (GB 50011-2010), sets the loading time of 20 h to model the damage process caused by an earthquake accurately, by repeating the loading procedure to replicate the effects of an actual earthquake, and analyzes the deformation before and after the earthquake.

2.2   Data acquisition and processing

On the basis of 3D LiDAR scanning technology,[31] we used a FARO Focus XD130 LIDAR scanner with an accuracy of 2 mm for point cloud data acquisition [Fig. 2(a)]. The specific technical parameters of the LIDAR scanner are shown in Table 1.

Additionally, on the basis of the principles of close-range photogrammetry, the DJI Jingling PHANTOM 4 RTK UAV with a maximum resolution of 20 MP was employed as the research object, the technical parameters of which are shown in Table 2. The process involves capturing images from multiple directions [Fig. 2(b)], guaranteeing a navigational overlap of 80% and a sideways overlap of more than 70%. The SfM algorithm was used to determine the original camera position, applying beam leveling and other techniques, and finally solving for null triples to create a dense point cloud and an image model with accurate color texture.

(a)   (b)

Fig. 2.   (Color online) Data collection site photos: (a) 3D LiDAR scanning and (b) close-range UAV.

Table 1
Technical parameters of FARO Focus XD130.

Parameter	Unit	Range
Pixel	Pix	70 million
Optical resolution	dpi	600 × 1200
Scanning range	°/°	Horizontal 360, Vertical360
Scanning distance	m	0.6–330
Maximum resolution	°/°	Vertical: 0.009, Horizontal: 0.009
Scanning speed	point/s	976000
Ranging error	mm	±2
Temperature parameter	°C	5–40 °C

Table 2
Technical parameters of RTK UAV.

Parameter	Unit	Range
Hover accuracy	m	Vertical: ±0.1 Horizontal: ±0.1
Satellite positioning modulev	cm	Vertical: 1.5 Horizontal: 1.5
Pixel	pix	20 million
Photo resolution	–	5472 × 3078 4864 × 3648 5472 × 3648

The data acquisition process was conducted in two stages. The first stage involved acquiring the 3D LiDAR point cloud and UAV photogrammetry images of the research object in its original state before the earthquake-resistant behavior test [Fig. 3(a)]. The second stage involved acquiring the 3D LiDAR point cloud and UAV photogrammetry images of the research object after it was deformed by the earthquake-resistant behavior test, specifically with the addition of a vertical slit steel plate [Fig. 3(b)]. These data sets were then used to analyze the deformation of the hybrid frame structural body before and after the test. The obtained data findings are shown in Fig. 4.

3.   Methods and Technology

3.1   Multifeature constraints for overall multisite cloud alignment

Research efficiency is enhanced to mitigate the cumulative error caused by multistation transmission, enhance data quality, and reduce the time spent on data processing. In this study, we utilized the high-precision control network as the benchmark constraint, employing the iterative closest point (ICP) technique introduced by Besl and McKay in 1992.[32] By considering the characteristics of points, lines, and surfaces in multisite cloud data and their mutual constraints, we employed the indirect leveling theory to determine the initial values for the station attitude and unknown point coordinates. Using these initial values, we performed iterative calculations with a weight function that incorporates each constraint error. This weight function serves as a constraint to achieve a solution for all the point cloud data. This overall solution is represented by

$$
\begin{aligned}
&\underset{3m\times1}{V_1} = \underset{3m\times k}{A_1}\ \underset{6k\times1}{t}\ +\ \underset{3m\times 3m}{B}\ \underset{3m\times1}{X}\ -\ \underset{3m\times1}{L_1} \\
&\underset{(4n+5l)\times1}{V_2} = \underset{(4n+5l)\times6k}{A_2}\ \underset{6k\times1}{t}\ \pm\ \underset{(4n+5l)\times1}{L_2}
\end{aligned}
\tag{1}
$$

Equation (2) represents the unified result, where k is the number of stations in the aligned point cloud, m is the number of point constraint features, n is the number of surface constraints, and l indicates the line constraints.

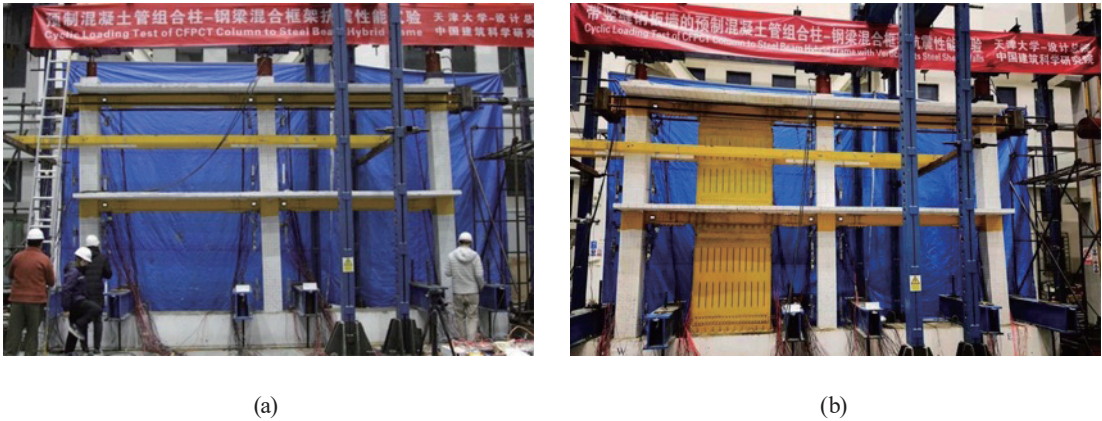(a)   (b)

Fig. 3.   (Color online) Hybrid frame structure before and after test: (a) hybrid frame structure before test and (b) hybrid frame structure with vertical slit steel plate after test.

(a)   (b)

(c)   (d)
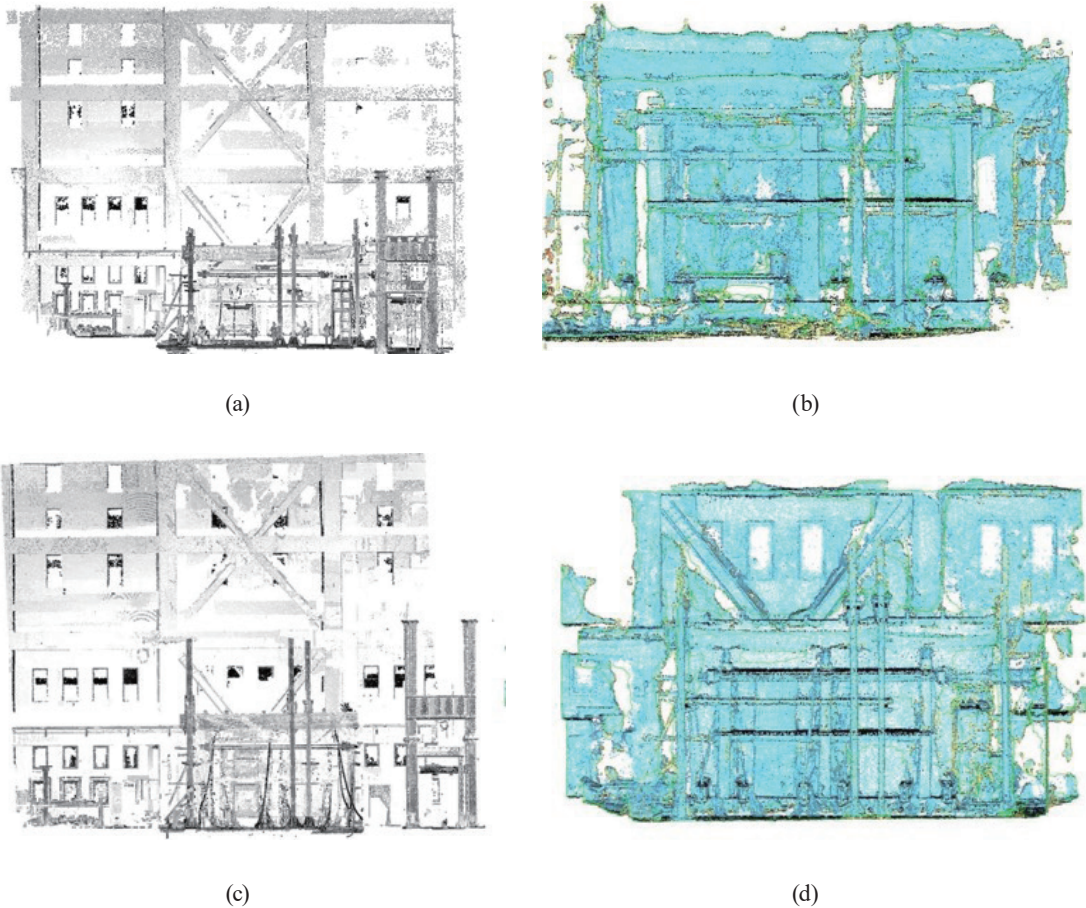
Fig. 4.   (Color online) Comparison of initial point clouds in two phases: (a) 3D LiDAR scanning point cloud of first phase, (b) UAV photogrammetry point cloud of first phase, (c) 3D LiDAR scanning point cloud of second phase, and (d) UAV photogrammetry point cloud of second phase.

$$V = At + BX - L$$

$$V = \begin{bmatrix} V_1 \\ V_2 \end{bmatrix}, A = \begin{bmatrix} A_1 \\ A_2 \end{bmatrix}, B = \begin{bmatrix} B_1 \\ 0 \end{bmatrix}, L \begin{bmatrix} L_1 \\ L_2 \end{bmatrix} \tag{2}$$

The observation residual is denoted by V. The coefficient matrix of the spatial transformation parameter A represents the spatial transformation parameter. The correction number is denoted by t. The coefficient matrix of the to-be-determined point is represented by B. The to-be-determined point parameter is denoted by X. Lastly, the observation residual is denoted by L. Each constraint has varying degrees of influence, and the error weight P is used to create the error model of the joint solution, which is expressed in matrix form as

$$\begin{bmatrix} A_1^T P_1 A_1 + A_2^T P_2 A_2 & A_1^T P_1 B \\ B^T P_1 B & D^T P B_1 \end{bmatrix} \begin{bmatrix} t \\ X \end{bmatrix} - \begin{bmatrix} A_1^T P_1 L_1 + A_2^T P_2 L_2 \\ B^T P_1 L_1 \end{bmatrix} = 0. \tag{3}$$

To ensure the rigor of the pilot study, before the point cloud alignment of the two phases of data, no pruning is performed on the point cloud data except for denoising, the objects without spatial position transformation and deformation are used as the alignment benchmark, and the relatively fine and complete point cloud data are selected as the reference base for the deformed objects to be aligned.

3.2 Selection and registration of homonymous points of two-phase data

To mitigate human error and prevent data accuracy loss, the point cloud is not thinned before aligning the two-phase data. The alignment method involves selecting the reference area near the research object but not included in the test image. The homonymous points are chosen on the basis of their prominence and visibility to prevent significant systematic errors caused by the deformation shift of these points. Such errors can interfere with the accurate analysis of the model and reduce its reliability and precision.

The main principle of the two-phase data alignment is as follows: first, the rotation angles ε_x, ε_y, and ε_z, the translations ΔX, ΔY, and ΔZ, and the scale factor σ are solved, so as to calculate the rotation matrix R and the translation matrix T when the target model is transformed. The coordinates of the vertex information after the deformation are set to be $[xyz]^T$, those of the vertex information before the deformation are set to be $[XYZ]^T$, and the transformation formula for the rotational transformation is given as

$$\begin{bmatrix} X \\ Y \\ Z \end{bmatrix} = \sigma R \begin{bmatrix} x \\ y \\ z \end{bmatrix} + \sigma T. \tag{4}$$

First, calculate the scale factor σ. The ratio of the corresponding side lengths is back-calculated from the coordinates of two homonymous points selected in both coordinate systems as

$$\sigma = \left(\frac{(X_{a2} - X_{a1})^2 + (Y_{a2} - Y_{a1})^2 + (Z_{a2} - Z_{a1})^2}{(X_{b2} - X_{b1})^2 + (Y_{b2} - Y_{b1})^2 + (Z_{b2} - Z_{b1})^2} \right)^{\frac{1}{2}}. \tag{5}$$

From the basic principle of the Rodriguez matrix,[33] in the process of transforming the coordinates, there exists an anti-symmetric matrix S. The anti-symmetric and rotation matrices are related as follows, where I is a third-order unit matrix as

$$R = (I + S)(I - S)^{-1}. \tag{6}$$

The anti-symmetric matrix can be represented by the three parameters in the Rodriguez matrix as

$$S = \begin{bmatrix} 0 & -\gamma & -\beta \\ \gamma & 0 & -\alpha \\ \beta & \alpha & 0 \end{bmatrix}. \tag{7}$$

At this point, the rotation matrix R is the Rodriguez matrix, whose expression can be expressed as Eq. (8). It can be seen that only the parameters should be solved to find the rotation matrix R. From this, the rotation matrix solver model is utilized to solve for the parameters. In solving, at least six equations are required and thus at least three homonymous point pairs are required for solving.

$$R = \frac{1}{\alpha^2 + \beta^2 + \gamma^2 + 1} \begin{bmatrix} 1 + \alpha^2 - \beta^2 - \gamma^2 & -2\gamma - 2\alpha\beta & -2\beta + 2\alpha\gamma \\ 2\gamma - 2\alpha\beta & 1 + \alpha^2 + \beta^2 - \gamma^2 & -2\alpha - 2\beta\gamma \\ 2\beta + 2\alpha\gamma & 2\alpha - 2\beta\gamma & 1 - \alpha^2 - \beta^2 + \gamma^2 \end{bmatrix} \tag{8}$$

The translation matrix T ($T = [\Delta X \Delta Y \Delta Z]^T$) can be solved by solving the obtained rotation matrix. After substituting the rotation matrix into Eq. (4), the translation parameters are finally obtained by averaging the multiple sets of translation parameters obtained, i.e., Eq. (10) (where n is the number of homonymous point pairs).

$$\begin{bmatrix} \Delta X \\ \Delta Y \\ \Delta Z \end{bmatrix} = \begin{bmatrix} X \\ Y \\ Z \end{bmatrix} - \frac{1}{\alpha^2 + \beta^2 + \gamma^2 + 1} \begin{bmatrix} 1 - \alpha^2 - \beta^2 - \gamma^2 & -2\gamma - 2\alpha\beta & -2\beta + 2\alpha\gamma \\ 2\gamma - 2\alpha\beta & 1 + \alpha^2 + \beta^2 - \gamma^2 & -2\alpha - 2\beta\gamma \\ 2\beta - 2\alpha\gamma & 2\alpha - 2\beta\gamma & 1 - \alpha^2 - \beta^2 + \gamma^2 \end{bmatrix} \begin{bmatrix} x \\ y \\ z \end{bmatrix} \quad (9)$$

$$T = \begin{bmatrix} \Delta X & \Delta Y & \Delta Z \end{bmatrix}^T = \frac{\sum_{i=1}^{n} ([X_n Y_n Z_n]^T - R[x_n y_n z_n]^T)}{n} \quad (10)$$

In aligning the two-phase data model, we picked nine pairs of homonymous points [Fig. 4(a)] to create the error equations and solve the parameters. This allowed us to successfully determine the rotation matrix *R* and the translation matrix *T*. As shown in Fig. 5, two reference regions were used to pick nine pairs of homonymous locations. We selected nine pairs of homonymous points from two reference regions. The first region is the part of the wall in the test space that did not experience any deformation during the earthquake-resistant behavior test. We chose six corner points that were easily visible through scanning. The second region is the load-bearing wall portion on the right side of the study object, where we selected three visible corner points. The nine chosen points with identical names exhibit well-defined boundaries around them and can serve as a reliable foundation for comparison. Furthermore, selecting distinct reference locations can enhance the precision of data alignment across the two phases and establish a calibration foundation for reciprocal validation.

3.3 Removal of redundant interference point clouds

In this study, we utilized a dispersive scanning 3D LiDAR scanner, which exhibits a wide scanning range and characteristics such as a multipath effect. In scanning, numerous objects surrounding the research target cause interference. This interference affects the analysis of the

(a)   (b)
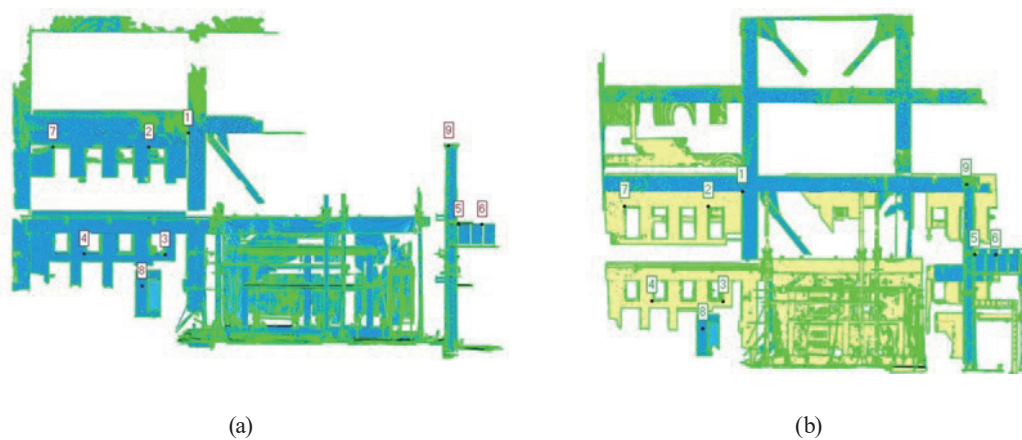
Fig. 5.   (Color online) Manual alignment of two-phase scan data: (a) first and (b) second phases.

point cloud's peripheral features and ambient noise. Therefore, it is necessary to remove this point cloud manually and only retain the point cloud of the area being studied for subsequent 3D deformation analysis. The manual removal of the point cloud is necessary, retaining only the point cloud of the specific area of interest for later 3D deformation analysis. The point clouds of the research item, excluding the interfering point clouds, are depicted in Fig. 6.

3.4   3D reconstruction based on UAV photogrammetry

To determine the 3D depth of the experimental scene and research object from multiangle true-color 2D images, we utilized the 3D depth information obtained from images captured by the Elf IV UAV. The 3D structure is then projected onto a series of images from various viewpoints for 3D reconstruction using the SfM algorithm. The primary components consist of two sections: matching search (which involves feature extraction, matching, and geometric verification) and incremental reconstruction (which includes initialization, picture alignment, triangulation, and beam technique leveling). The 3D reconstruction outcomes are achieved by inputting several photos.

It is necessary to set up and calibrate the camera before data acquisition and provide the calibration images from different angles for input, then convert the world coordinate system to the image coordinate system to address the camera's internal and external parameters. From various perspectives, capturing many 2D photographs of the research object and its surroundings is necessary using true-color technology. The SIFT feature detection operator is utilized to extract and describe the feature points of an image.

Additionally, image stereo correction is necessary to ensure that the images are aligned in the same plane and level. This correction involves calculating the relative rotation matrix R and the relative translation vector T of the camera's external parameters. Subsequently, the 3D coordinates of the point to be measured are determined by utilizing the geometric relationship between triangles. This is achieved by employing the known internal and external characteristics of the camera and the image point coordinates of the feature points in various photographs. Subsequently, the methods employed, such as SfM and beam leveling, are utilized to restore the

(a)   (b)
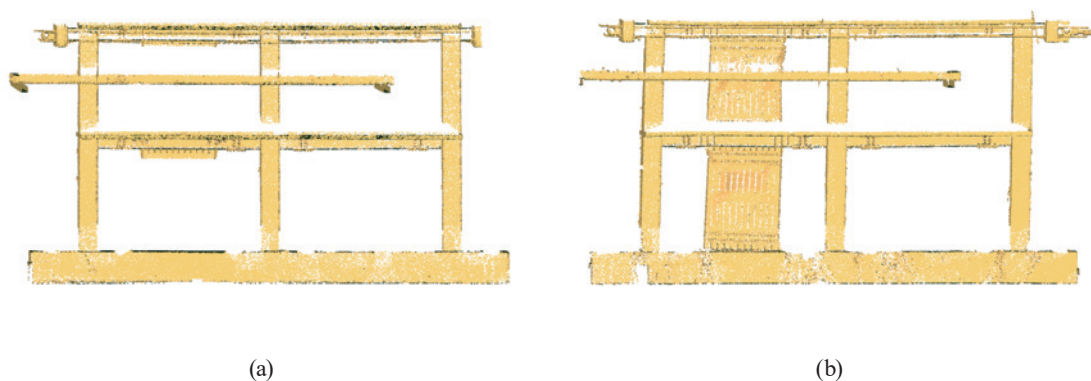
Fig. 6.   (Color online) Scanning structural body point cloud (a) before and (b) after experimentation.

original camera position. This enables the subsequent 3D reconstruction of the study object; the result is shown in Fig. 7.

3.5   3D reconstruction based on 3D LiDAR scanning

In this study, we used a surface reconstruction approach, specifically the 3D Delaunay triangular mesh,[34] to create a 3D model of a laser radar point cloud. The technique does surface extraction on the sampled points obtained during scanning (mapping the item in 3D space) to acquire an appropriate topology for building the initial Delaunay triangular mesh structure.

Given the extensive data obtained through the 3D scanning technique and numerous factors that can cause interference, creating a satisfactory surface model is impractical. Therefore, it becomes essential to divide the vast number of point clouds into smaller sections and employ algorithms within each section to construct the model. Following the construction process, block-to-block splicing is carried out to achieve a surface reconstruction structure that exhibits enhanced precision and improved integrity.

The effectiveness of surface reconstruction algorithms heavily depends on the quality of the point cloud data. A denser and more accurate point cloud enables the algorithm to be used more effectively. However, in reality, several uncertainties result in a limited number of sampling sites. This also poses a challenge for specific algorithms that rely on the sampled points' standard information to compute the data for mesh generation appropriately. The 3D Delaunay algorithm exhibits superior adaptability, even in minor point cloud omissions. Nevertheless, it can produce a more comprehensive, transparent, and superior result than the other algorithms for the triangular mesh model (Fig. 8).
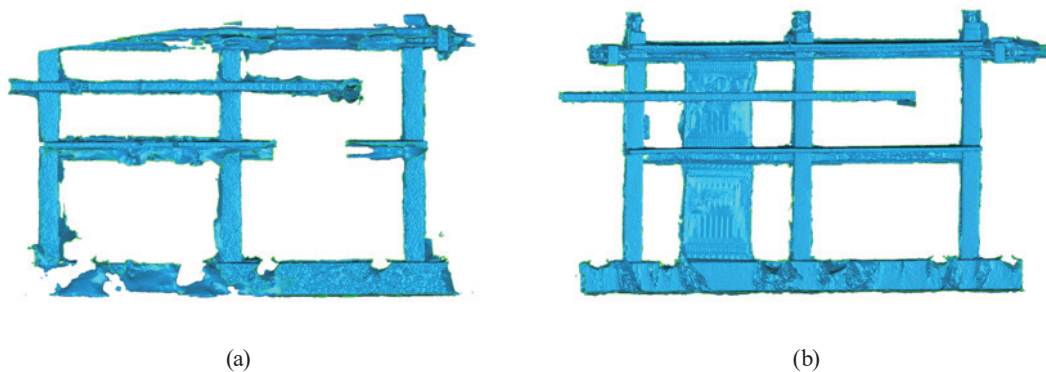

(a)   (b)

Fig. 7.   (Color online) Comparison of photogrammetric reconstruction model in two phases: (a) first and (b) second phases.

<div align="center">(a)   (b)</div>

Fig. 8.   (Color online) Comparison of 3D LiDAR scanning triangular grid model in two phases: (a) first and (b) second phases.

4   Results and Discussion

4.1   Result analysis

4.1.1 3D deformation analysis based on UAV photogrammetry

The UAV photogrammetry collects 2D truecolor images of the research object and its surrounding features. These images are obtained using photogrammetry, which converts 2D image data into 3D models. The collected data are then used for comparison by creating 3D solid models. The method also allows for the analysis of 3D deformation by comparing the data collected before and after the test. The results of this analysis are shown in Fig. 9.

The statistics include the maximum positive deviation value of 0.8547 m and the maximum negative deviation value of −0.8700 m. The average positive deviation value is 0.8547 m, and the average negative deviation value is −0.1458 m. The standard deviation value is 0.2141 m, as shown in Fig. 10.

4.1.2   3D deformation analysis based on 3D LiDAR scanning

When assessing the extent of deformation on the surface of a hybrid frame structure, the inaccuracy resulting from manual measurement is significant. It does not allow for obtaining measurements of deformation within the structure. In this study, we utilized the initial phase point cloud model as a reference point and compared it with the subsequent phase model after the seismic test. The 3D analysis ribbon diagrams generated from this comparative analysis [Fig. 11(a)] offer a more accurate and visually precise observation of the deformation of the hybrid frame structure body. The green portion represents the deformation offset unaffected by the test.

Conversely, the deformed section is mainly characterized by transverse micro-deformation, with its primary structure inclined towards the right rear. Notable distortions are present at specific connecting nodes and edges [Figs. 11(b) and 11(c)]. Nevertheless, the deformation of the structure is consistent throughout, indicating that the earthquake-resistant performance of this mixed-frame construction is generally stable and has a solid basis for withstanding seismic

(a)

(b)   (c)
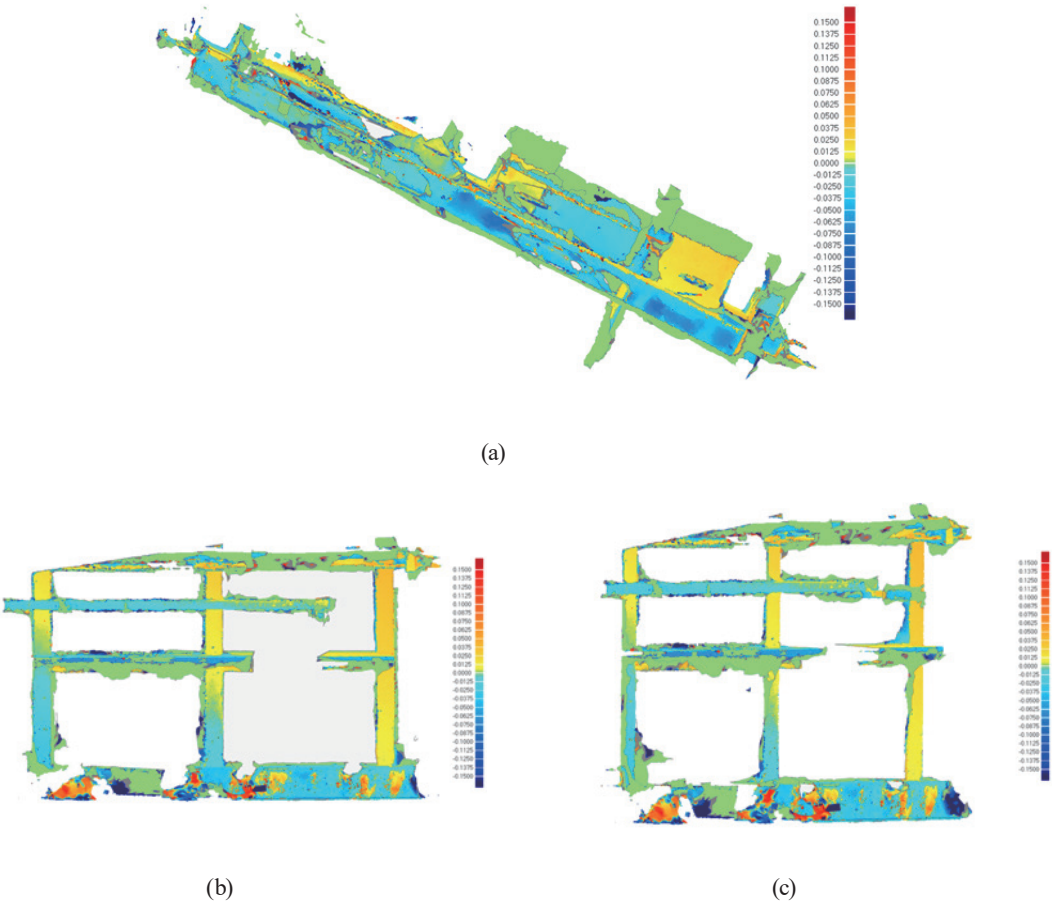
Fig. 9.   (Color online) UAV photogrammetry based 3D deformation analysis results: (a) top, (b) front, and (c) side views.
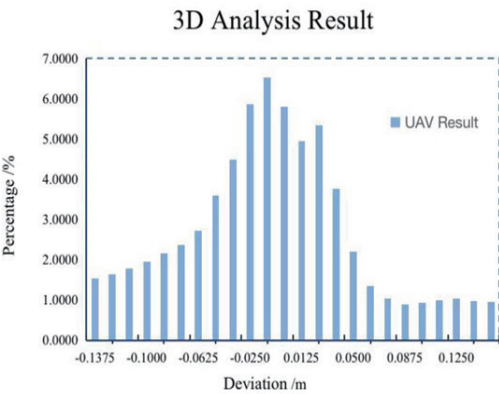

Fig. 10.   (Color online) Deviation diagram for 3D deformation analysis of two-phase data from UAV photogrammetry.

(a)

(b)   (c)
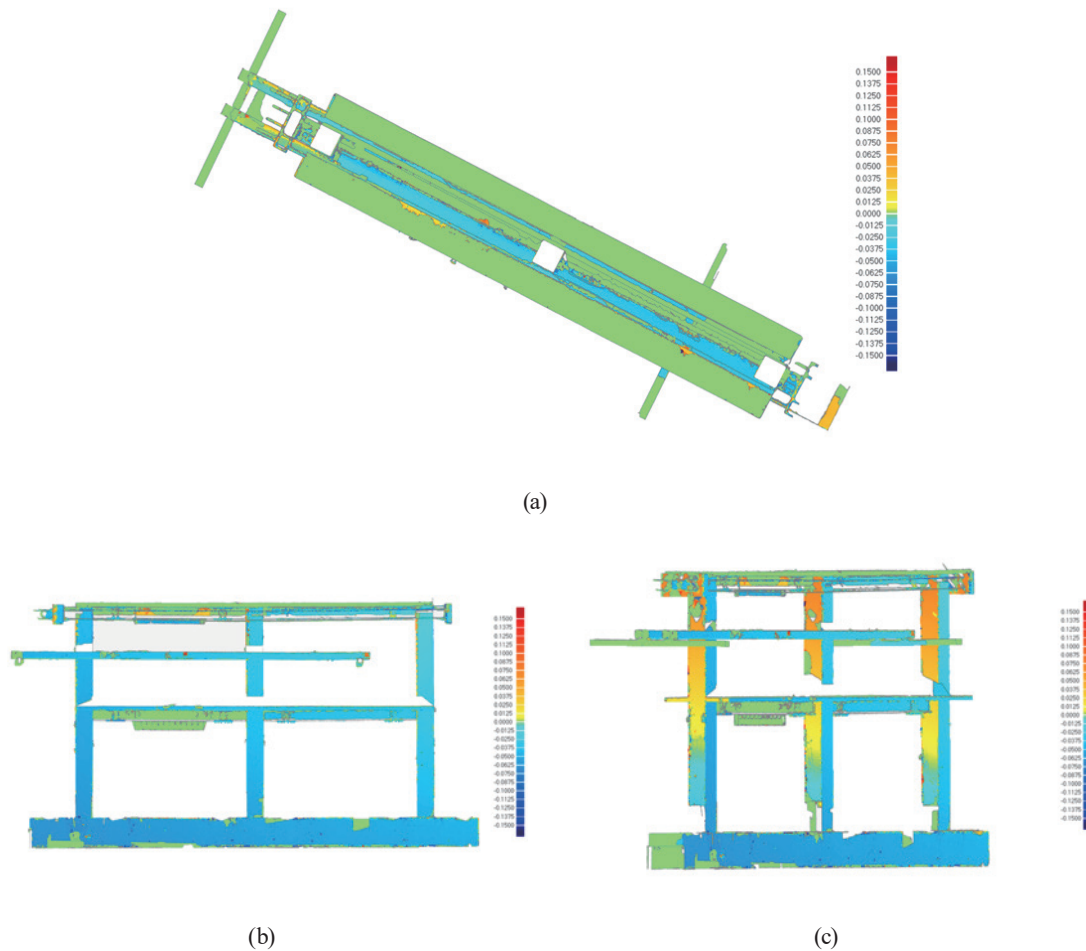
Fig. 11.   (Color online) 3D LiDAR based 3D deformation analysis results: (a) top, (b) front, and (c) side views.

activity. Additionally, a vertical slit steel plate is incorporated into the structure, creating a twofold anti-side-standing system. This design enhances the structural body's elasticity and optimizes the utilization of the material and the structural body's maximum advantages.

Through the 3D analysis and comparison of experimental statistics, we obtained data on the maximum positive deviation value (0.3900 m), maximum negative deviation value (−0.3900 m), average positive deviation value (0.0796 m), average negative deviation value (−0.600 m), and standard deviation value (0.0936 m). These results are illustrated in Fig. 12.

4.2   Comparison of data acquisition methods and accuracy analysis

4.2.1   Analysis of advantages and disadvantages of two data collection methods

Our primary research data sources are photogrammetry images captured by UAV and point cloud data obtained through 3D LiDAR scanning. The images captured by UAVs were processed
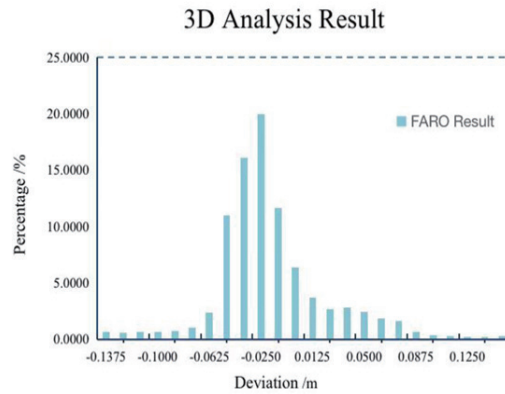
Fig. 12.   (Color online) Deviation diagram for 3D deformation analysis of two-phase data from 3D LiDAR scanning.

using the SfM algorithm to generate a 3D model with accurate color representation. The 3D Delaunay surface reconstruction algorithm was also used to construct a 3D point cloud model.

UAVs are compact, facilitating effortless assembly and portability while also being user-friendly, effectively fulfilling most operators' data collection requirements. Simultaneously, the 3D LiDAR scanning technology gathers extensive data from reliable sources. Aside from the measurement station's initial setup, adjusting the tripod's height, and configuring the parameters, no further modifications are necessary during the acquisition process. Moreover, manual operation will not have any detrimental effects on it.

However, it is crucial to guarantee optimal lighting conditions and a consistent illumination surface while gathering data from a drone. Additionally, capturing many photographs is necessary to construct a more intricate model. Assume that an obstructing object is present during data collection. Consequently, the model obtained after data processing will exhibit phenomena where a portion of its structure is missing (Fig. 13). This is attributed to the limitations of the UAV camera, which fails to capture a sufficiently broad view angle. The precision of the measurements is diminished near the ground. The existing algorithms exhibit flaws, particularly in delineating the model boundaries and the portion of the ground adjacent to the surface. This lack of clarity hinders the study of the structural body's earthquake-resistant behavior.

Before data collection by the 3D LiDAR scanner, the user can specify the data density, allowing for scanning findings that are more closely aligned with the specific study objectives. Furthermore, 3D LiDAR technology gathers extensive data, enabling a more accurate depiction of the surrounding environment. However, this also necessitates a more significant amount of data processing. The presence of obstructing objects along the path of the laser emission will lead to data loss in the veiled portion of the research object. As a result of the limitations of UAV photogrammetry, such as a narrow field of view and low accuracy when capturing images close to the ground, the 3D LiDAR scanning used in this study provides a higher data accuracy than UAV photogrammetry. Additionally, the research data collected through 3D LiDAR scanning is more stable and comprehensive, as depicted in Fig. 14.

Fig. 13. (Color online) Ribbon diagram of 3D deformation analysis of two phases of UAV photogrammetry data.
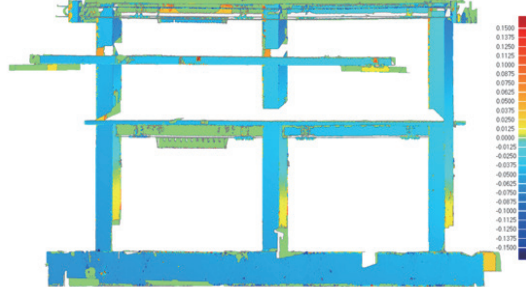

Fig. 14. (Color online) Ribbon diagram of 3D deformation analysis of two phases of 3D LiDAR scanning data.

Table 3
Standard deviations for comparison of data from two phases.

UAV Photogrammetry			3D LiDAR Scanning		
$\geq$ Min	< Max	Percent(%)	$\geq$ Min	< Max	Percent(%)
−0.1500	−0.1375	1.5276	−0.1500	−0.1375	0.6224
−0.1375	−0.1250	1.6328	−0.1375	−0.1250	0.5783
−0.1250	−0.1125	1.7763	−0.1250	−0.1125	0.6044
−0.1125	−0.1000	1.9419	−0.1125	−0.1000	0.6555
−0.1000	−0.0875	2.1566	−0.1000	−0.0875	0.7279
−0.0875	−0.0750	2.3585	−0.0875	−0.0750	0.9953
−0.0750	−0.0625	2.7177	−0.0750	−0.0625	2.3342
−0.0625	−0.0500	3.5913	−0.0625	−0.0500	10.9898
−0.0500	−0.0375	4.4855	−0.0500	−0.0375	16.0752
−0.0375	−0.0250	5.8507	−0.0375	−0.0250	19.9885
−0.0250	−0.0125	6.5237	−0.0250	−0.0125	11.6516
−0.0125	0.0000	5.7943	−0.0125	0.0000	6.3437
0.0000	0.0125	4.9414	0.0000	0.0125	3.6803
0.0125	0.0250	5.3320	0.0125	0.0250	2.6263
0.0250	0.0375	3.7560	0.0250	0.0375	2.7980
0.0375	0.0500	2.1991	0.0375	0.0500	2.4035
0.0500	0.0625	1.3349	0.0500	0.0625	1.8497
0.0625	0.0750	1.0249	0.0625	0.0750	1.5965
0.0750	0.0875	0.8845	0.0750	0.0875	0.6707
0.0875	0.1000	0.9211	0.0875	0.1000	0.3244
0.1000	0.1125	0.9812	0.1000	0.1125	0.2678
0.1125	0.1250	1.0330	0.1125	0.1250	0.1885
0.1250	0.1375	0.9625	0.1250	0.1375	0.1882
0.1375	0.1500	0.9428	0.1375	0.1500	0.2385

4.2.2 Accuracy analysis of deformation analysis results

To better understand the pros and cons of the deformation analysis results from the two data acquisition methods before and after the seismic test, we utilized the analyzed data to create Table 3, showing the distribution of standard deviations, as well as bar charts (Fig. 15). Through observation and comparison, it is evident that UAV photogrammetry exhibits a higher degree of
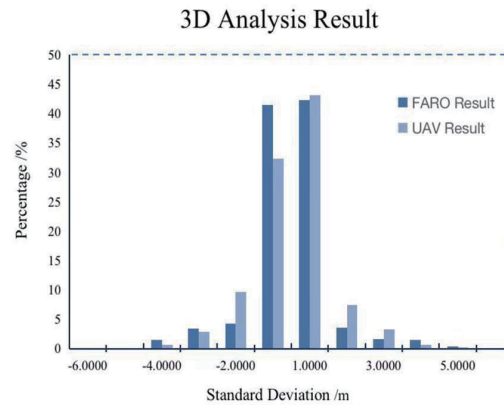
Fig. 15.   (Color online) Distribution of standard deviation of deformation analysis by different methods.

fluctuating deviation and a lower level of stability in the analysis of deformation findings from the two data collection stages, compared with 3D LiDAR scanning. The precision of the deformation analysis outcomes obtained from the model created by UAV photogrammetry is inferior to that of 3D LiDAR scanning. The primary cause for this outcome is an excessive presence of obstructing entities surrounding the subject of study. A meticulous roping procedure is necessary for data processing to eliminate interfering items outside the hybrid frame structure. This operation causes the structural body to become partially absent, leading to insufficient analysis of deformation objects.

5.   Conclusion

To address the issues of incomplete data and ambiguous feature descriptions resulting from a single sensor, we utilized the combined capabilities of UAV photogrammetry and 3D LiDAR observation technology for data acquisition and deformation analysis on the hybrid frame consisting of manufactured concrete pipes and steel beams. An advanced alignment algorithm enhances the precision and effectiveness of aligning UAV photogrammetry images. This algorithm combines point, line, and surface features. Additionally, a dense point cloud generation algorithm based on SfM is utilized to achieve 3D-reconstructed close-range photogrammetry images. The Rodriguez matrix was employed to align the two-phase data before and after the earthquake-resistant behavior test to assist in investigating deformation in the hybrid frame construction. We utilized UAV to gather image data, enabling a more precise acquisition of model features and texture data. This facilitated the visualization of structural deformation and allowed for focused analysis and comparison of severe offset areas between two data phases. A high-precision 3D LiDAR scanning technique was employed to obtain a 3D point cloud model. The scanning accuracy was carefully controlled to within 2 mm to minimize accuracy loss. The resultant 3D reconstruction can significantly enhance the precision of the model and align it more closely with the real-world conditions of the hybrid frame structure, hence boosting the accuracy of the deformation analysis.

We conducted comparative, qualitative, and quantitative analyses to obtain deformation data between two phases obtained under the UAV photogrammetry method for the manufactured concrete pipe combined column-steel beam hybrid frame and the deformation data obtained on the basis of 3D LiDAR scanning. The following conclusions were drawn:

(1) We found that the accuracy of data obtained through 3D LiDAR scanning is superior to that of UAV photogrammetry. Additionally, the data obtained in the study are more stable and substantially more comprehensive.

(2) Prior to and following the earthquake-resistant behavior test, the hybrid frame structure experienced a significant shift towards the right rear. This resulted in substantial deformation at the nodes and edges and extensive bending deformation and bending-shear cracks at the top of the columns. The columns also exhibited severe deflection, and there was noticeable crushing at the connection between the columns and the concrete beds. Despite these damages, the overall structure did not collapse and remained relatively stable post-test.

In earthquake disasters, building collapse is one of the major causes of casualties, so rapid assessment of the extent of building damage is important for emergency management and rescue. In this study, we provided a feasible method for the deformation analysis before and after the earthquake disaster of buildings: the data were collected using the UAV and 3D LiDAR, which can be complementary to each other for their respective shortcomings and serve as a reliable basis for the sensor data to make a more comprehensive data supplement. The collection duration of this method in this experiment is 6 h in total, which requires less labor, but the data processing and analysis are more time-consuming. The accuracy is mainly dependent on the accuracy of the alignment algorithm, which can be applied to the field of the structural deformation analysis of buildings in actual earthquake scenarios with higher accuracy and contributing to earthquake relief and mitigation of disaster damage and casualties in the future.

Acknowledgments

References

1 A. Sagradyan, N. Ogura, and T. Shiotani: Dev. Built Environ. **14** (2023) 100127. https://doi.org/10.1016/j.dibe.2023.100127

2 L. Candido and F. Micelli: Bull. Earthquake Eng. **16** (2018) 4107. https://doi.org/10.1007/s10518-018-0325-9

3 K. B. Ramkumar, K. R. Pr, and K. Gunasekaran: Eng. Sci. Technol. **42** (2023) 101432. https://doi.org/10.1016/j.jestch.2023.101432

4 P. Derakhshesh, S. R. Mirghaderi, G. Nouri, and M. Farzam: J. Constr. Steel Res. **210** (2023) 108043. https://doi.org/10.1016/j.jcsr.2023.108043

5 S. Tang, P. Li, and F. Zhao: Corros. Prot. **42** (2021) 66. https://doi.org/10.11973/fsyfh-202109013

6 G. Nouri, A. Rayegani, H. H. Lavasani, L. Tavakoli, M. Nasiri, and O. K. Soureshjani: Structures **56** (2023) 105003. https://doi.org/10.1016/j.istruc.2023.105003

7 P. Martnez-Carricondo, F. Agera-Vega, and F. Carvajal-Ramrez: Remote Sens.-Basel. **12** (2020) 2221. https://doi.org/10.3390/rs12142221

8 J. Siwiec and G. Lenda: Measurement **199** (2022) 111404. https://doi.org/10.1016/j.measurement.2022.111404

9　T. Luhmann, M. Chizhova, D. Gorkovchuk, H. Hastedt, N. Chachava, and N. Lekveishvili. Int. Arch. Photogramm. Remote Sens. Spatial Inf. Sci. (2019) 753. https://doi.org/10.5194/isprs-archives-XLII-2-W11-753-2019019

10　M. Guo, X. Tang, Y. Liu, C. Wang, and Y. Wei: Opt. Precis. Eng. **31** (2023) 1988. https://doi.org/10.37188/OPE.20233113.1988

11　I. Zhao, P. Yuan, X. Zhang, and T. Zheng: J. Xi'an Polytechnic University **35** (2021) 7. https://doi.org/10.13338/j.issn.1674-649x.2021.03.009

12　J. Wang, T. Yi, X. Liang, and T. Ueda: Remote Sens.-Basel **15** (2023) 64. https://doi.org/10.3390/rs15010064

13　Z. Gao, G. Wang, M. Guo, and T. Zhou: Bull. Surv. Mapp. (2020) 151. https://doi.org/10.13474/j.cnki.11-2246.2020.0063

14　M. Guo, T. Shao, C. Gao, and J. Zhao: Sci. Surv. Mapp. (2020) 7. https://doi.org/10.16251/j.cnki.1009-2307.2020.02.013

15　Y. Zhao, M. Guo, and X. Duan: Construction Quality **1** (2014) 3. https://doi.org/10.3969/j.issn.1671-3702.2014.01.002

16　J. Zhang, J. Huang, C. Fu, L. Huang, and H. Ye: Constr. Build Mater. **270** (2021) 121402. https://doi.org/10.1016/j.conbuildmat.2020.121402

17　M. Li, L. Cheng, J. Gong, Y. Liu, Z. Chen, F. Li, G. Chen, D. Chen, and X. Song: Sci. China Ser. E-Technol. Sci. **51** (2008) 133. https://doi.org/10.1007/s11431-008-6014-1

18　F. Yang, X. Wen, X. Wang, X. Li, and Z. Li: Adv. Civ. Eng. **2021** (2021) 5542012. https://doi.org/10.1155/2021/5542012

19　A. Pesci, G. Teza, E. Bonali, G. Casula, and E. Boschi: ISPRS J. Photogrmm. **79** (2013) 185. https://doi.org/10.1016/j.isprsjprs.2013.02.021

20　F. Foroughnia, V. Macchiarulo, L. Berg, M. DeJong, P. Milillo, K. W. Hudnut, K. Gavin, and G. Giardina: Int. J. Disaster Risk Reduct. **106** (2024) 104403. https://doi.org/10.1016/j.ijdrr.2024.104403

21　A. Federman, S. Shrestha, M. Santana Quintero, D. Mezzino, J. Gregg, S. Kretz, and C. Ouimet: Drones-Basel **2** (2018) 18. https://doi.org/10.3390/drones2020018

22　M. Guo, Z. Fu, D. Pan, Y. Zhou, M. Huang, and K. Guo: Meas. Control **55** (2022) 555. https://doi.org/10.1177/00202940221110949

23　B. Yang, F. Ali, B. Zhou, S. Li, Y. Yu, T. Yang, X. Liu, Z. Liang, and K. Zhang: Comput. Electr. Eng. **99** (2022) 107804. https://doi.org/10.1016/j.compeleceng.2022.107804

24　A. Jasiska, K. Pyka, E. Pastucha, and H. S. Midtiby: Sens.-Basel **23** (2023) 728. https://doi.org/10.3390/s23020728

25　J. Shan, H. Zhu, and R. Yu: Struct. Control Health Monit. **2023** (2023) 7743762. https://doi.org/10.1155/2023/7743762

26　R. Yu, P. Li, J. Shan, and H. Zhu: Measurement **202** (2022) 111858. https://doi.org/10.1016/j.measurement.2022.111858

27　R. Zhang, H. Li, K. Duan, S. You, K. Liu, F. Wang, and Y. Hu: Remote Sens.-Basel **12** (2020) 2621. https://doi.org/10.3390/rs12162621

28　N. Jiang, H. B. Li, C. J. Li, H. X. Xiao, and J. W. Zhou: IEEE Trans. Geosci. Remote Sens. **60** (2022) 1. https://doi.org/10.1109/TGRS.2022.3181258

29　Z. Liu and G. Gu: Hydrographic Surveying and Charting (2018). https://doi.org/CNKI:SUN:HYCH.0.2018-05-009

30　J. L. Schonberger and J.-M. Frahm. 2016 IEEE Conf. Computer Vision and Pattern Recognition. (IEEE, 2016) 4104−4113. https://doi.org/10.1109/CVPR.2016.445

31　M. Zhou, H. Wang, G. Wang, M. Guo, and Y. Liu: Geotech. Invest. Surv. **48** (2020) 6. https://doi.org/CNKI:SUN:GCKC.0.2020-05-010

32　P. J. Besl and H. D. Mckay: IEEE. T. Pattern. Anal. **14** (1992) 239. https://doi.org/10.1109/34.121791

33　S. Zhang: Geomatics and Information Science of Wuhan University **01** (1987) 81. https://doi.org/CNKI:SUN:WHCH.0.1987-01-007

34　J. Jia, M. Huang, and X. Liu: Acta. Geod. Cartogr. Sin **47** (2018) 281. https://doi.org/10.11947/j.AGCS.2018.2017049

About the Authors

Ming Guo is a professor and Ph.D. supervisor of Beijing University of Civil Engineering and Architecture. He received his Ph.D. degree from Wuhan University's State Key Laboratory of Remote Sensing Information Engineering in 2011. He serves as a reviewer for the Chinese National Natural Science Foundation and renowned domestic and international SCI journals, including Automation in Construction. He focuses primarily on 3D GIS research and LIDAR technology use. His research interests include building health monitoring, LiDAR mapping technology, and the digital preservation of cultural assets. (guoming@bucea.edu.cn)

Xuan Shuo Liang received his B.S. degree from Beijing University of Civil Engineering and Architecture, China, in 2023. He is currently studying for his M.S. degree from the Architectural Heritage Digitization Lab, which is part of the School of Geomatics and Urban Spatial Informatics at Beijing University of Engineering and Architecture. His research interests are in LiDAR mapping technology, the digital twin, 3D reconstruction, and the digital protection of cultural heritage. (2098679880@qq.com)

You Shan Zhao is from Nanyang, Henan, and he works at the China Academy of Building Research Co., Ltd. He earned his master's degree in cartography and geographic information engineering from Beijing University of Engineering and Architecture in 2008. His primary field of work is structural inspection. (yshzhao@163.com)

Guo Li Wang received his B.S. degree in 2004 from China University of Mining and Technology, his M.S. degree in 2007 from Beijing University of Engineering and Architecture, China, and his Ph.D. degree in 2011 from Wuhan University, China. From 2011 until recently, he worked at Beijing University of Engineering and Architecture, China. His research interests are in the automated processing of ground LiDAR data, refined city modeling, smart city, and so forth. (wangguoli@bucea.edu.cn)

Ke Cai Guo from Wuhan, Hubei, is a senior engineer. He received his B.S. degree from Ezhou University in 2006. He is currently the General Manager of Beijing Shenxindacheng Technology Co., Ltd., and is mainly engaged in research on mobile LiDAR scanning, engineering measurement, and automation technology. (1033547194@qq.com)